



Article

Carbonaceous Materials in the Fault Zone of the Longmenshan Fault Belt: 1. Signatures within the Deep Wenchuan Earthquake Fault Zone and Their Implications

Li-Wei Kuo ^{1,*} , Jyh-Rou Huang ², Jiann-Neng Fang ³, Jialiang Si ⁴ , Haibing Li ⁴ and Sheng-Rong Song ⁵

¹ Department of Earth Sciences, National Central University, Taoyuan 320, Taiwan

² Department of Earth Sciences, National Taiwan Normal University, Taipei 106, Taiwan; hjrou0906@hotmail.com

³ National Taiwan Museum, Taipei 100, Taiwan; jnfang@ntm.gov.tw

⁴ Institute of Geology, Chinese Academy of Geological Sciences, Beijing 100037, China; gongrenbaqin@126.com (J.S.); lihaibing06@163.com (H.L.)

⁵ Department of Geosciences, National Taiwan University, Taipei 106, Taiwan; srsong@ntu.edu.tw

* Correspondence: liweikuo@ncu.edu.tw; Tel.: +886-3-4227151 (ext. 65628)

Received: 22 June 2018; Accepted: 3 September 2018; Published: 4 September 2018



Abstract: Graphitization of carbonaceous materials (CM) has been experimentally demonstrated as potential evidence of seismic slip within a fault gouge. The southern segment of the Longmenshan fault, a CM-rich-gouge fault, accommodated coseismic slip during the 2008 Mw 7.9 Wenchuan earthquake and potentially preserves a record of processes that occurred on the fault during the slip event. Here, we present a multi-technique characterization of CM within the active fault zone of the Longmenshan fault from the Wenchuan earthquake Fault Scientific Drilling-1. By contrast with field observations, graphite is pervasively and only distributed in the gouge zone, while heterogeneously crystallized CM are present in the surrounding breccia. The composite dataset that is presented, which includes the localized graphite layer along the 2008 Wenchuan earthquake principal slip zone, demonstrates that graphite is widely distributed within the active fault zone. The widespread occurrence of graphite, a seismic slip indicator, reveals that surface rupturing events commonly occur along the Longmenshan fault and are characteristic of this tectonically active region.

Keywords: graphitization; graphite; Longmenshan fault; Wenchuan earthquake; WFSD-1

1. Introduction

Graphitization is a progressive and irreversible transformation from disordered carbonaceous materials (CM) into stable ordered graphite and can occur under a wide variety of conditions (e.g., [1]). Current studies propose that graphitization of CM is facilitated with confining pressure, burial time, temperature, fluid, and shear stress/strain [2–6]. In particular, increasing temperature on CM has been commonly suggested to cluster carbon atoms and grow graphite [7], and the associated characteristics of CM are widely utilized to estimate the maximum temperatures achieved in sedimentary and metamorphic rocks [6,8]. Because CM are also a common constituent within fault rocks, it seems likely that the stable structure of carbon and its relevant graphitization among different fault components (e.g., damage zone and fault core) can be studied to gain insights into faulting mechanisms [9].

The NE–SW trending Longmenshan thrust fault ruptured on 12 May 2008 in a devastating Mw 7.9 earthquake near Wenchuan in SE Tibet, producing a 240 km-long Yingxiu–Beichuan surface rupture and an 80 km-long Guanxian–Anxian surface rupture, respectively (Figure 1a) [10]. Both field observations and the Wenchuan earthquake Fault Scientific Drilling project-1 (WFSD-1) along the Yingxiu–Beichuan surface rupture reported the presence of CM within the active fault zone of the southern Longmenshan fault, presumably derived from the Triassic Xujiahe formation sedimentary rocks (coal-bearing sandstone) [11–15]. Therefore, this provides a unique opportunity to link seismic fault motions and the relevant gouge graphitization by integrating the evidence of CM from the field and laboratory.

Kouketsu et al. [15] characterized the naturally and experimentally deformed (at slip rates of 0.1–2.1 m/s and normal stresses of 0.6–2.1 MPa) CM-bearing gouge of the surface outcrop of the southern Longmenshan fault, and suggested that graphite was likely formed extremely locally or not formed during the seismic fault motion because of the lack of the evidence of graphitization processes adjacent to surrounding rocks. Kuo et al. [16], however, conducted rock friction experiments on the CM-rich fault gouge of the WFSD-1 (at a slip rate of 3 m/s and normal stresses of 5–25 MPa) and characterized experimentally deformed products, suggesting that gouge graphitization processes likely occurred within the active fault zone of the Longmenshan fault during the 2008 Mw 7.9 Wenchuan earthquake. In addition, on the basis of the extended experimental conditions (at slip rates of 0.0003 to 3 m/s, a normal stress of 8.5 MPa, and room-humidity and water-damped conditions), Kuo et al. [17] experimentally demonstrated that graphitization of CM can be induced by high-temperature pulses associated to seismic slip. The geological records of the active fault zone of the Longmenshan fault from the surface outcrop show the absence of graphite [15], but those from the active fault zone of the WFSD-1 remain largely unknown, and so other evidence and the associated graphitization for seismic slip must be determined and developed.

Here, we present a detailed characterization of graphitization of CM within the Longmenshan fault recovered from the WFSD-1. The CM-rich gouges were found in the fault core including the recognized 2008 Wenchuan principal slip zone (PSZ) [16,17]. By means of micro-Raman spectroscopy and transmission electron microscopy (TEM), we establish a reference graphitization of a CM data set of the recent-event slipping fault zone, address the geological record of the fault-relevant graphitization, discuss the differential graphitization from surface outcrop to deep depth and, by extension, present an application of these data for studies of exhumed CM-bearing fault segments in tectonically active regions without determined earthquake records.

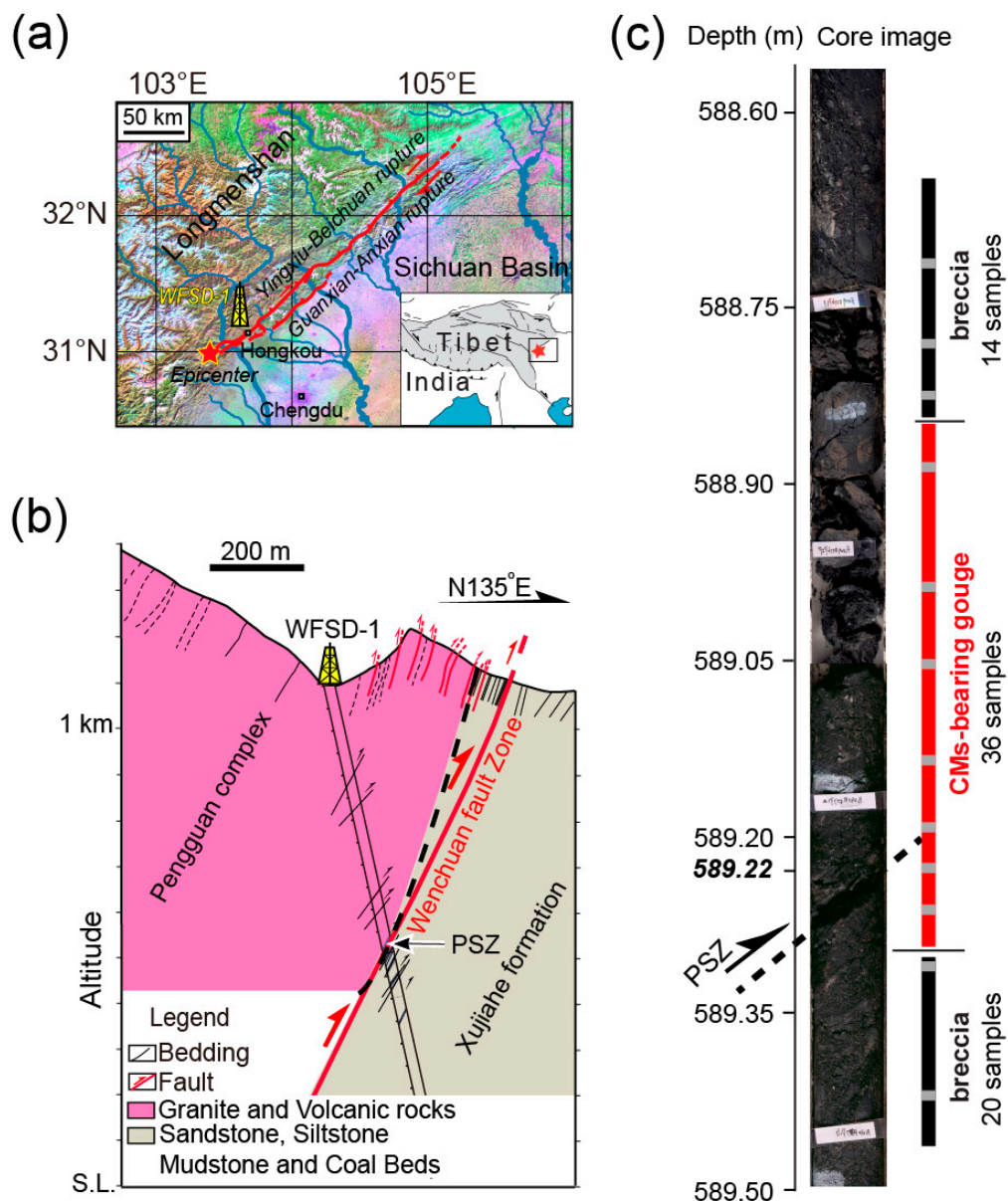


Figure 1. Geological setting of the 2008 Mw 7.9 Wenchuan earthquake, China, and location of the Wenchuan earthquake Fault Scientific Drilling project-1 (WFSD-1) drilling site, marking the major fault zone. (a) The 240 km-long Yingxiu–Beichuan surface rupture and the 80 km-long Guanxian–Anxian surface rupture associated with the Mw 7.9 earthquake along the margin of the Longmenshan fault belt, and the location of WFSD-1 drilling site. Red star represents epicenter of the main shock. Inset is a schematic plot of the Tibetan Plateau. (b) An E135° W cross section of the WFSD-1 showing the Wenchuan fault zone and surrounding formations encountered in the borehole [11]. The arrow indicating the principal slip zone active during the 2008 mainshock was identified in the borehole at 589.22 m depth and the images of fault core samples of the WFSD-1 was enlarged in the right panel as (c). (c) The core image exhibiting major portions of the Longmenshan fault along the borehole of WFSD-1 including breccia and gouge. Grey rectangles showing the location of samples analyzed by Kuo et al. [17].

2. Materials and Methods

The WFSD-1 drilled to a depth of 1201.1 m around 40 km north-east of the epicentral area (Figure 1a) and passed through the boundary of the Neoproterozoic Pengguan complex (diorite,

porphyrite, volcanic rocks and pyroclastics) and the Triassic Xujiahe Formation sedimentary rocks (coal-bearing sandstone) at a depth of 585.7 m in total width of 19.8 m, broadly marking the location of the Longmenshan fault zone (Figure 1b) [11]. The structural analysis of the recovered borehole materials indicated that the Longmenshan fault contains a narrow “fault core” surrounded by a broad “damage zone” mainly within the Xujiahe Formation [11,18]. The current description of the WFSD-1 fault core shows a number of recurring elements such as one or several slip surfaces, fractures, fault rocks (e.g., gouge and breccia), and lenses of protolith of fault rock [11]. On the basis of both geological and geophysical observations of the WFSD-1, the PSZ accommodated coseismic displacement during the 2008 Wenchuan earthquake was proposed at the depth of 590 m (Figure 1c) [11,12,16,19].

The detailed phyllosilicate data of the WFSD-1 has been established by analyzing 139 samples within the boundary of the Pengguan complex and Xujiahe formation. In particular, the clay-size fraction (<2 micrometers) from 82 samples that were 1 cm-thick was sequentially analyzed across the active fault zone of the Longmenshan fault, including 17 samples from the hanging wall damage zone, 43 samples within the fault core, and 22 samples from the foot wall damage zone [12]. Because of the presence of smeared CM within these samples [12], here we characterize the CM of the active fault zone by taking advantage of analyzing the 70 clay-size fraction samples collected from collected from the CM-rich gouge at 1-cm intervals, and integrate twelve samples reported in Kuo et al. [17]. Although Salver-Disma et al. [20] demonstrated that the structure of CM can be damaged by mechanical grinding after duration of more than 20 h, damage on CM by gentle crushing during short sample preparation (less than 20 min) can be likely ignored in our case.

We directly obtained the Raman spectra of CM from clay-size fraction samples deposited on glass slides with a Horiba Jobin Yvon ultraviolet–visible (UV–VIS) Labram HR Micro-Raman spectrometer (HORIBA, Kyoto, Japan) at the National Taiwan Museum. We performed Raman experiments with an excitation beam of wavelength of 532 nm and a laser power of 5 mW without neutral density filters, and focused in the 1100–1800 cm^{-1} region of the Raman spectrum which includes the first-order bands of CM: the G (from 1575 cm^{-1} –1592 cm^{-1}), the D1 (from 1330 cm^{-1} –1336 cm^{-1}) and the D3 (from 1490 cm^{-1} –1525 cm^{-1}) bands (Figure 2a inset). In Raman spectroscopy, the sharpness of peak of the D1 (defect) band and the G (graphite) band is widely utilized to quantify the degree of the graphitization process [5,6]. Therefore, we utilized the commercial software PeakFit 4.12 (Systat Software, Inc., San Jose, CA, USA) for fitting peaks of both G and D1 bands with the pseudo-Voigt function (Gaussian–Lorentzian linear combination) [21,22], and calculated the following parameters: peak intensity (maximum of height), peak width (at half maximum of height), and peak position (frequency, cm^{-1}) (Figure 2a inset) [17]. Ten measurements per sample were conducted on different sample spots, and each spot was measured with three integration times of 5 s. The spectral parameters (G and D1) of each sample were determined as the on-average values of 10 Raman analyses. The spectrum of Raman analysis was calibrated with a Si-waver prior to each set of measurement. The curve-fitting in our study is likely influenced by an individual operator and might be processed with a standardized curving-fitting procedure as suggested by Lünsdorf [23,24] in the future.

To determine crystal structures and chemical composition of CM derived from different fault components, we analyzed the breccia and gouge samples collected from depths of 588.70 m and 589.23 m, respectively. The clay-size fraction samples were disaggregated in ethanol and deposited on a Cu supporting grid for TEM. We performed TEM equipped with an energy dispersive X-ray spectrometer (TEM-EDX) analysis in the FEI Tecnai G2 T20 TEM and Philips Tecnai F30 Field Emission Gun TEM (Thermo Fisher, Waltham, MA, USA) with accelerating voltages of the electron beam which were 200 KV and 300 KV, respectively. Selected-area electron diffraction (SAED) patterns were taken using the selected-area aperture to obtain the electron diffraction pattern of CM.

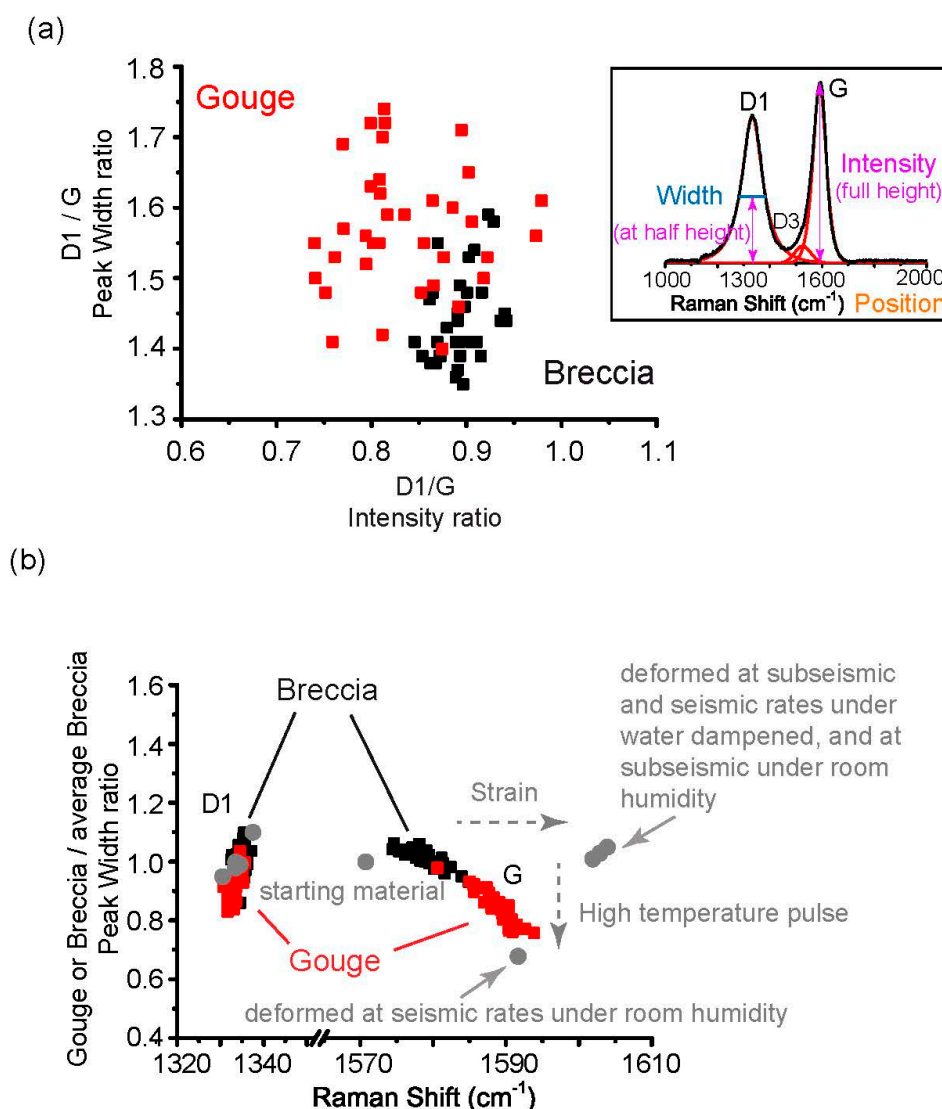


Figure 2. Raman spectra of WFS-1 samples. (a) D1/G peak width ratio versus D1/G intensity ratio. The inset shows a representative first-order region of Raman spectrum and defines the indicative parameters derived from the relevant spectrum decomposition (width, intensity, peak position, etc.). (b) D1 or G peaks width of gouge over average breccia peak width versus D1 and G band peak position. Grey circles representing the experimental results obtained from Kuo et al. [17], and the grey dashed arrows showing the variation of Raman spectra after rock friction experiments under varied ambient conditions and slip rates, attributing to strain and high temperature pulses.

3. Results

In this study we use two indicative parameters of CM introduced in Kuo et al. [17]: (1) the D1/G width ratio versus D1/G intensity ratio (Figure 2a), and (2) the D1 and G widths (normalized by the average D1 and G widths of the breccia) versus their peak position (Figure 2b). The gouge samples, compared to the breccia samples, have a widely distributed cluster of D1/G intensity ratio and D1/G width ratio (Figure 2a; Table 1). Importantly, the gouge and breccia samples have similar D1 band position and peak width ratio, but most of the G band of the gouge has higher frequency and smaller peak width ratio (Figure 2b; Table 1). Integrated with the reported phyllosilicate mineral (the abundance of smectite; [12]), a summary diagram with the indicative parameters of CM is shown in Figure 3. The occurrence and characterization of the CM are discussed below.

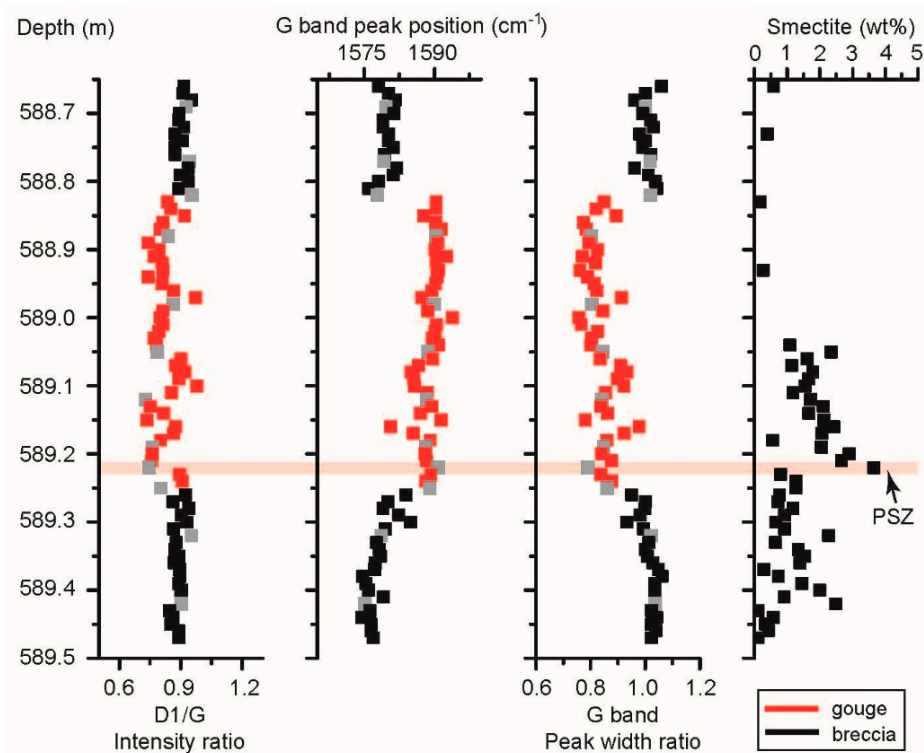


Figure 3. Raman spectra of WFSD-1 samples across the Wenchuan fault zone, including the recognized 2008 Mw 7.9 Wenchun principal slip zone (PSZ). Grey rectangles representing the location of analyzed samples by Kuo et al. [17]. The reported phyllosilicate mineral (the abundance of smectite; [12] Si et al., 2014) is integrated in the right panel, showing the location of the PSZ.

The CM of the breccia samples, showing essentially the presence of strong diffuse rings in the corresponding electron diffraction patterns, sometimes intimately mixed with crystallized spots, are confirmed as poorly crystalline (Figure 4a,b and Figure 5). Although the strong diffuse rings resembling crystallized spots are also presenting in the CM of the gouge samples (Figures 4c and 5), the presence of perfectly well-ordered carbon-built grains, likely suggesting the transformation of CM into graphite (Figures 4d and 5), is only obtained in the gouge samples.

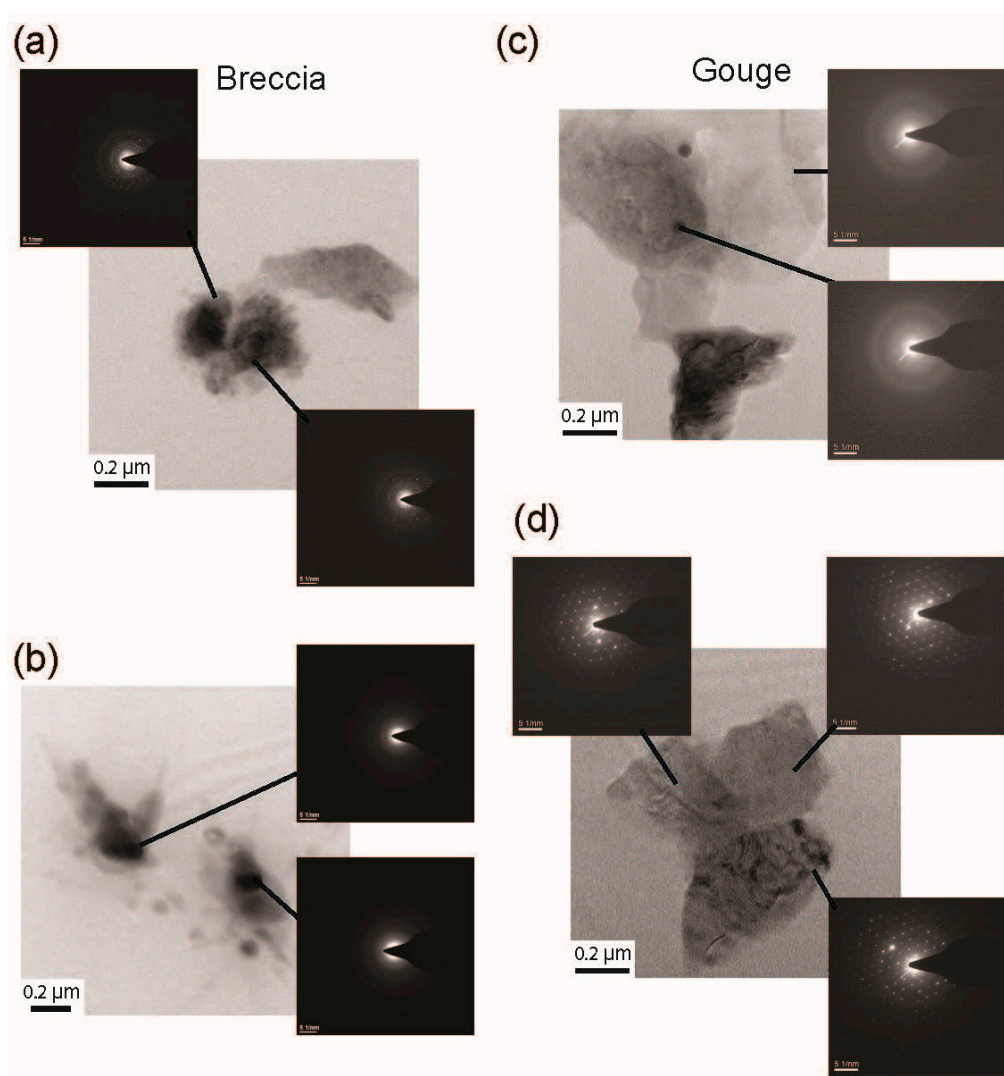


Figure 4. Microstructures of carbonaceous materials of both breccia (at the depth of 588.70 m) and gouge (at the depth of 589.23 m). (a,b) Poorly ordered carbon grains (see selected-area electron diffraction (SAED) patterns) within the breccia samples (transmission electron microscope (TEM) images). (c,d) poorly ordered to well crystallized carbon grains (see SAED patterns) within the gouge samples (TEM images).

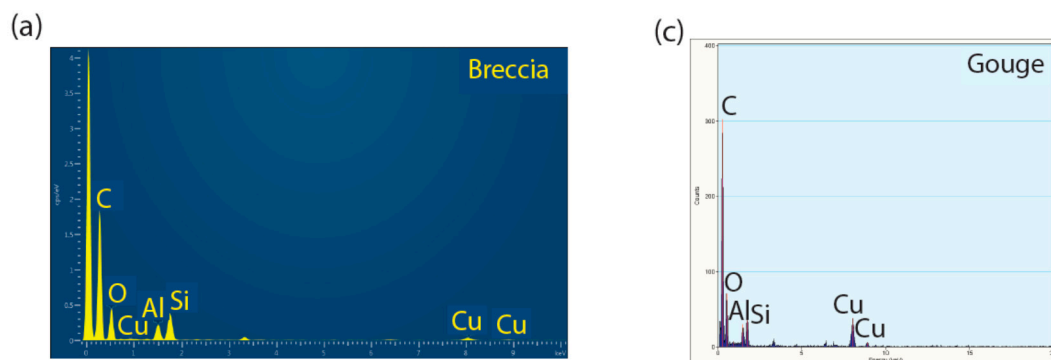


Figure 5. Cont.

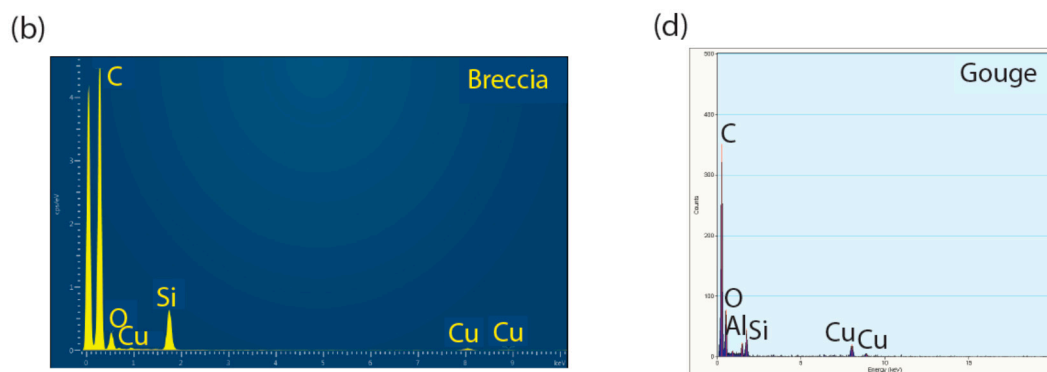


Figure 5. TEM energy-dispersive X-ray spectroscopy (TEM-EDX) analyses on breccia samples and gouge samples. (a,b) TEM-EDX of the breccia samples showing that the selected-area electron diffraction (SAED; Figure 4a,b in the main text) is on-average composed of carbon (91.2 and 95.07 wt%, respectively) as the dominant element, whereas sub-elements are copper (0.98 and 0.49 wt%, respectively) (TEM grid), silicon (4.9 and 4.4 wt%, respectively) and aluminum (2.92 and 0.04 wt%, respectively). (c,d) TEM-EDX of the gouge samples showing that the SAED (Figure 4c,d in the main text) comprises of on-average carbon (87 and 93 wt%, respectively) as the dominant element, whereas sub-elements are oxygen (8 and 4.9 wt%, respectively), silicon (2.5 and 0.6 wt%, respectively), and aluminum (2.5 and 1.5 wt%, respectively).

Table 1. Results of spectra decomposition along the depths for breccia and gouge of the active Wenchuan earthquake fault zone from the WFSD-1.

Type	Depth (m)	D1/G intensity (Error Estimate ± 0.06)	D1/G Width Ratio (Error Estimate ± 0.09)	Peak Position (cm^{-1})		Gouge or Breccia/ Average Breccia	
				D1	G	D1	G
Breccia	588.66	0.92	1.48	1336	1578	1.1	1.1
Breccia	588.67	0.91	1.41	1335	1580	1.0	1.0
Breccia	588.68	0.95	1.28	1335	1582	0.9	1.0
Breccia	588.70	0.89	1.49	1337	1581	1.0	1.0
Breccia	588.71	0.89	1.37	1336	1579	1.0	1.0
Breccia	588.72	0.91	1.39	1336	1579	1.0	1.0
Breccia	588.73	0.87	1.39	1335	1580	0.9	1.0
Breccia	588.74	0.91	1.54	1335	1580	1.1	1.0
Breccia	588.75	0.87	1.55	1336	1581	1.1	1.0
Breccia	588.76	0.87	1.39	1334	1579	1.0	1.0
Breccia	588.77	0.94	1.44	1335	1579	1.0	1.0
Breccia	588.79	0.90	1.46	1336	1581	1.0	1.0
Breccia	588.80	0.94	1.44	1336	1578	1.0	1.0
Breccia	588.81	0.89	1.36	1334	1576	1.0	1.0
Gouge	588.83	0.83	1.59	1334	1590	0.95	0.85
Gouge	588.84	0.85	1.48	1333	1590	0.85	0.82
Gouge	588.85	0.92	1.5	1334	1588	0.94	0.89
Gouge	588.86	0.81	1.7	1331	1590	0.92	0.77
Gouge	588.87	0.80	1.63	1333	1591	0.89	0.79
Gouge	588.89	0.74	1.5	1332	1591	0.83	0.79
Gouge	588.90	0.79	1.52	1333	1590	0.87	0.82
Gouge	588.91	0.77	1.69	1333	1593	0.91	0.77
Gouge	588.92	0.81	1.62	1333	1590	0.93	0.82
Gouge	588.93	0.81	1.72	1331	1591	0.91	0.76
Gouge	588.94	0.74	1.55	1332	1591	0.85	0.79
Gouge	588.95	0.81	1.64	1333	1590	0.93	0.81
Gouge	588.96	0.86	1.61	1334	1589	0.92	0.82
Gouge	588.97	0.97	1.56	1336	1587	1.00	0.91
Gouge	588.99	0.81	1.42	1333	1589	0.84	0.85
Gouge	589.00	0.80	1.72	1334	1594	0.91	0.76

Table 1. Cont.

Type	Depth (m)	D1/G intensity (Error Estimate ± 0.06)	D1/G Width Ratio (Error Estimate ± 0.09)	Peak Position (cm^{-1})		Gouge or Breccia/ Average Breccia	
				D1	G	D1	G
Gouge	589.01	0.81	1.74	1332	1590	0.93	0.77
Gouge	589.02	0.79	1.56	1333	1590	0.90	0.82
Gouge	589.03	0.77	1.57	1332	1590	0.88	0.80
Gouge	589.04	0.89	1.6	1333	1591	0.90	0.80
Gouge	589.06	0.90	1.65	1335	1590	0.96	0.83
Gouge	589.07	0.88	1.53	1335	1587	0.97	0.91
Gouge	589.08	0.92	1.53	1334	1585	1.00	0.93
Gouge	589.09	0.89	1.46	1334	1586	0.91	0.90
Gouge	589.10	0.98	1.61	1334	1586	1.04	0.92
Gouge	589.11	0.85	1.55	1333	1588	0.93	0.85
Gouge	589.13	0.75	1.48	1333	1589	0.86	0.84
Gouge	589.14	0.82	1.59	1332	1587	0.95	0.86
Gouge	589.15	0.81	1.55	1332	1591	0.84	0.78
Gouge	589.16	0.87	1.4	1333	1581	0.96	0.98
Gouge	589.17	0.87	1.49	1334	1585	0.96	0.92
Gouge	589.18	0.80	1.55	1334	1589	0.93	0.86
Gouge	589.20	0.76	1.53	1333	1588	0.90	0.84
Gouge	589.21	0.76	1.41	1334	1588	0.86	0.88
Gouge	589.23	0.89	1.71	1334	1589	1.00	0.84
Gouge	589.24	0.91	1.58	1335	1588	0.97	0.88
Breccia	589.26	0.92	1.59	1334	1584	1.06	1.0
Breccia	589.27	0.86	1.47	1335	1580	1.03	1.0
Breccia	589.28	0.94	1.45	1334	1579	1.01	1.0
Breccia	589.29	0.90	1.53	1336	1582	1.05	1.0
Breccia	589.30	0.93	1.58	1334	1585	1.02	0.9
Breccia	589.31	0.86	1.48	1334	1579	1.02	1.0
Breccia	589.33	0.88	1.43	1335	1578	1.01	1.0
Breccia	589.34	0.87	1.41	1334	1578	0.99	1.0
Breccia	589.35	0.89	1.41	1334	1578	0.99	1.0
Breccia	589.36	0.87	1.38	1335	1577	0.99	1.0
Breccia	589.37	0.89	1.39	1335	1577	1.02	1.0
Breccia	589.38	0.90	1.35	1333	1575	1.00	1.1
Breccia	589.39	0.89	1.41	1333	1575	1.02	1.0
Breccia	589.40	0.90	1.41	1334	1576	1.02	1.0
Breccia	589.41	0.90	1.48	1336	1579	1.07	1.0
Breccia	589.43	0.85	1.41	1334	1576	1.01	1.0
Breccia	589.44	0.86	1.38	1333	1574	1.01	1.0
Breccia	589.45	0.85	1.39	1333	1576	0.99	1.0
Breccia	589.46	0.89	1.45	1334	1577	1.05	1.0
Breccia	589.47	0.89	1.44	1334	1577	1.03	1.0

4. Discussion and Conclusions

Kuo et al. [17] carried out rock friction experiments on the CM-rich gouge of WFSD-1 at a normal stress of 8.5 Mpa and at both sub-seismic (0.0003 m/s) and seismic (3 m/s) slip rates under room-humidity and water-damped conditions to investigate graphitization of CM. Amorphous CM are composed of two types of the electronic configuration of the carbon atoms: sp^3 (diamond-like) and sp^2 (graphite-like). Graphitization of CM is the conversion of the sp^2 -bond from sp^3 -bond and turned into graphite as the end product [25]. The D1/G peak intensity ratio is proposed to be inversely proportional to the average size of the sp^2 clusters from conversion of sp^3 bonds [25]. Kuo et al. [17] characterized the experimentally deformed CM-rich gouge of the WFSD-1, showing the G band shifts toward higher frequencies in both the gouges sheared at sub-seismic and seismic slip rates. This suggests that bulk shear strain triggers the transformation of sp^2 -bond carbon from sp^3 -bond carbon in the amorphous carbon network because of re-hybridization of interacting dangling bonds of carbon [26]. Therefore, Kuo et al. [17] suggested that graphitization of CM was attributed to bulk shear strain associated with a decreasing D1/G peak intensity ratio plus the G band peak position shifting towards higher frequency.

In addition, increasing temperature could facilitate the ordering phase of sp^2 and result in the formation of graphite [7], characterizing a smaller G band peak width [5]. Kuo et al. [17] estimated high temperatures (up to 300 °C) was achieved during frictional sliding at seismic slip rates and room-humidity conditions, accompanying the observed small width ratio of G bands and the presence of graphite. By contrast, water vaporization likely buffered the temperature increase (limited to less than 200 °C) and impeded the formation of graphite in the water-dampened experiments at seismic slip rates [27]. Therefore, Kuo et al. [17] suggested that transient high temperature pulses form graphite, showing a decreasing G band peak width ratio.

Similarly, our gouge samples, characterized by decreasing D1/G peak intensity ratio (Figure 2a; the Raman parameters and its interpretation are shown in grey color in Figure 2b) plus shift of G band peak position towards higher frequency (Figure 2b), showed the conversion of sp^3 -bond carbon (diamond-like carbon) into sp^2 -bond carbon (graphite-like carbon) and were likely graphitized by strain [3,23]. In addition, the smaller G peak width ratio of the gouge samples (Figure 2b), representing the increasingly crystallized CM (Figure 4d), was presumably derived from frictional heating produced by the seismic slip [17].

On the basis of the experimental conditions at which graphite forms [17], this suggests that the formation of graphite requires a certain amount of energy (strain and temperature) and at specific conditions, instead of high temperatures as suggested dominant parameters [6,8]. For instance, graphite was formed with the friction power density $>4 \text{ MW/m}^2$ [17] under water-deficient conditions, while at the same conditions the CM remain disordered with the friction power density $\sim 0.15 \text{ MW/m}^2$ [15,16]. In addition, integrated observation of the surface outcrop (the absence of graphite; [15]) and our results (the presence of graphite) suggest that frictional heat resulted from seismic slip can be efficiently generated at depth (e.g., higher effective normal stresses) and sufficiently triggers the graphitization of CM. Similar variation of frictional heating resulted from seismic slip along depth was observed in the Taiwan Chelungpu fault Drilling Project (TCDP) for the 1999 Chi-Chi Mw 7.6 earthquake: evidence of frictional heating derived from seismic slip was not found in the surface rupture of the Chelungpu fault [28,29], but was clearly obtained from the TCDP (e.g., [30–34]). Therefore, the state of gouge graphitization in our case, due to the stable structure of graphite, could be reliable evidence of ancient seismic faulting, if not due to precipitation from percolating thermal fluid [35]. It is notable that graphite within fault zones might be mechanically modified into relatively disorder graphite by brittle processes [36]. Indeed, findings from rock friction experiments suggest that graphitisation of CM in fault zones is a complex process [17,34,36].

Geological observation and rock friction experiments evidence that localization of slip and strain during an individual coseismic event forms a thin PSZ in depth ranging from a few hundred micrometers to a centimeter in thickness [37] and triggers physico-chemical processes [38], as was documented in the case in the nearby Mw 7.9 Wenchuan earthquake (e.g., graphitization within the $\sim 200 \text{ }\mu\text{m}$ -thick PSZ at the depth of 590 m; [16]). We integrated those features of the Wenchuan PSZ with the obtained microstructural and mineralogical characteristics of the CM-rich gouge from our study (Figure 3): localized shear strain seems to be heterogeneously distributed within the gouge zone because of the presence of widely distributed clusters of the D1/G intensity ratio (Figure 2a), presumably resulting from multiple seismic slips (Figures 2b and 4d). Coincidentally, the recognized PSZ corresponding to the 2008 Mw 7.9 Wenchuan earthquake [11,12] has almost the smallest values of D1/G intensity ratio and G band peak width ratio and a high-frequency shifting of G band within the active fault zone (Figure 3). If so, dozens of similar characteristics of approximately 1 cm-scale gouge zones are observed within the gouge zone of the WFSD-1, likely illustrating the occurrence of multiple previous slip events like the 2008 Mw 7.9 Wenchuan earthquake.

CM and graphite, derived from the conversion of sp^3 -bond carbon into sp^2 -bond carbon and the formation of graphite, have been demonstrated as lubricants [39–41]. Although fault slip within the gouge zone in a single earthquake resulting in graphitization of CM may be only at local patches or at asperity contacts along a fault surface, the formation of graphitic CM within the gouge zone would

likely reduce the fault's resistance to slip [40] and facilitate the development of PSZs which is considered a precursor for future earthquake slip [42]. That may provide a plausible interpretation for the evidence of multiple seismic slips recorded within the CM-rich gouge of the WFSD-1. However, we are unable to distinguish the thickness of CM-rich gouge deformed by the single coseismic event and further estimate the event numbers with the observed cumulative deformation evidence. Further systematic rock friction experiments on the CM-rich gouge are required to decipher fault slip behaviors and the associated microstructural evolution of the graphitized CM-rich gouge.

In summary, compared to the breccia samples (less deformed during earthquakes), the graphitization of CM of the WFSD-1 gouge is commonly characterized by a decreasing D1/G peak intensity ratio, a shift of G band peak position towards higher frequency, and a smaller G peak width ratio. The graphitization of CM, as suggested from the rock friction experiments by Kuo et al. [17], was attributed to bulk shear strain and transient frictional heating; the latter is associated with the smaller G peak width ratio in Raman spectra and results in the formation of graphite. Importantly, the pervasive occurrence of the graphite within the active fault zone may represent multiple seismic slip records as the consequence of rapid coseismic faulting and may act as precursors for future earthquake slip in the tectonically active Longmenshan fault belt.

Author Contributions: L.-W.K. wrote the paper; L.-W.K. conceived the present idea and planned the experiments; J.-R.H. conducted the experiments; L.-W.K., and J.-R.H. analyzed the data; J.-N.F., J.S., S.-R.S., and H.L. contributed materials and analysis tools; E.-C.Y. took part to the discussion. L.-W.K. coordinated the study.

Funding: This research used materials provided by the “WFSD” of the National Science and Technology Planning Project. Part of this work was supported by the National Science Foundation of China (41572192, 41330211, 41520104006) to Haibing Li, and Taiwan ROC (Republic of China) Ministry of Science and Technology (MOST 105-2628-M-008-002-MY3) and NCU grants to Li-Wei Kuo.

Acknowledgments: We thank the two anonymous reviewers, and Editor Chen for their positive and constructive comments.

Conflicts of Interest: The authors declare no conflict of interest.

References

1. Buseck, P.R.; Beyssac, O. From organic matter to graphite: Graphitization. *Elements* **2014**, *10*, 421–426. [[CrossRef](#)]
2. Rouzaud, J.-N.; Oberlin, A. Structure, microtexture, and optical properties of anthracene and saccharose-based carbons. *Carbon* **1989**, *27*, 517–529. [[CrossRef](#)]
3. Ross, J.V.; Bustin, R.M. The role of strain energy in creep graphitization of anthracite. *Nature* **1990**, *343*, 58–60. [[CrossRef](#)]
4. Bustin, R.M.; Ross, J.V.; Rouzaud, J.-N. Mechanisms of graphite formation from kerogen: Experimental evidence. *Int. J. Coal Geol.* **1995**, *28*, 1–36. [[CrossRef](#)]
5. Beyssac, O.; Rouzaud, J.N.; Goffé, B.; Brunet, F.; Chopin, C. Graphitization in a high-pressure, low-temperature metamorphic gradient: A Raman microspectroscopy and HRTEM study. *Contrib. Mineral. Petrol.* **2002**, *143*, 19–31. [[CrossRef](#)]
6. Beyssac, O.; Goffé, B.; Petit, J.P.; Froigneux, E.; Moreau, M.; Rouzaud, J.N. On the characterization of disordered and heterogeneous carbonaceous materials by Raman spectroscopy. *Spectrosc. Acta Part A* **2003**, *59*, 2267–2276. [[CrossRef](#)]
7. Thomas, P.; Delbe, K.; Himmel, D.; Mansot, J.L.; Cadore, F.; Guerin, K. Tribological properties of low-temperature graphite fluorides. Influence of the structure on the lubricating performances. *J. Phys. Chem. Solids* **2006**, *67*, 1095–1099. [[CrossRef](#)]
8. Barker, C.E.; Goldstein, R.H. Fluid-inclusion technique for determining maximum temperature in calcite and its comparison to the vitrinite reflectance geothermometer. *Geology* **1990**, *18*, 1003–1006. [[CrossRef](#)]
9. Oohashi, K.; Hirose, T.; Kobayashi, K.; Shimamoto, T. The occurrence of graphite-bearing fault rocks in the Atotsugawa fault system, Japan: Origins and implications for fault creep. *J. Struct. Geol.* **2012**, *38*, 39–50. [[CrossRef](#)]

10. Xu, X.; Wen, W.; Yu, G.; Klinger, Y.; Hubbard, J.; Shaw, J. Coseismic reverse- and oblique-slip surface faulting generated by the 2008 Mw7.9 Wenchuan earthquake, China. *Geology* **2009**, *37*, 515–518. [[CrossRef](#)]
11. Li, H.; Wang, H.; Xu, Z.; Si, J.; Pei, J.; Li, T.; Huang, Y.; Song, S.-R.; Kuo, L.-W.; Sun, Z.; et al. Characteristics of the fault-related rocks, fault zones and the principal slip zone in the Wenchuan earthquake Fault Scientific Drilling Hole-1 (WFSD-1). *Tectonophysics* **2013**, *584*, 23–42. [[CrossRef](#)]
12. Si, J.; Li, H.; Kuo, L.-W.; Pei, J.; Song, S.-R.; Wang, H. Clay mineral anomalies in the Yingxiu-Beichuan fault zone from the WFSD-1 drilling core and its implication for the faulting mechanism during the 2008 Wenchuan earthquake (Mw 7.9). *Tectonophysics* **2014**, *619–620*, 171–178. [[CrossRef](#)]
13. Wang, H.; Li, H.; Si, J.; Sun, Z.; Huan, Y. Internal structures of the Wenchuan earthquake fault zone, revealed by surface outcrop and WFSD-1 drilling core investigation. *Tectonophysics* **2014**, *619–620*, 101–114. [[CrossRef](#)]
14. Wang, Y.; Ma, S.; Shimamoto, T.; Yao, L.; Chen, J.; Yang, X.; He, H.; Dang, J.; Hou, L.; Togo, T. Internal structures and high-velocity frictional properties of Longmenshan fault zone at Shenxigou activated during the 2008 Wenchuan earthquake. *Earth Sci.* **2014**, *27*, 499–528. [[CrossRef](#)]
15. Kouketsu, Y.; Shimizu, I.; Wang, Y.; Yao, L.; Ma, S.; Shimamoto, T. Raman spectra of carbonaceous materials in a fault zone in the Longmenshan thrust belt, China; comparisons with those of sedimentary and metamorphic rocks. *Tectonophysics* **2017**, *699*, 129–145. [[CrossRef](#)]
16. Kuo, L.-W.; Li, H.; Smith, S.A.F.; Di Toro, G.; Suppe, J.; Song, S.-R.; Nielsen, S.; Sheu, H.-S.; Si, J. Gouge graphitization and dynamic fault weakening during the 2008 Mw 7.9 Wenchuan earthquake. *Geology* **2014**, *42*, 47–50. [[CrossRef](#)]
17. Kuo, L.-W.; Di Felice, F.; Spagnuolo, E.; Di Toro, G.; Song, S.-R.; Aretusini, S.; Li, H.; Suppe, J.; Si, J.; Wen, C.-Y. Fault gouge graphitization as evidence of past seismic slip. *Geology* **2017**, *45*, 979–982. [[CrossRef](#)]
18. Li, H.; Xu, Z.; Niu, Y.; Kong, G.; Huang, Y.; Wang, H.; Si, J.; Sun, Z.; Pei, Z.; Gong, Z.; et al. Structural and physical property characterization in the Wenchuan earthquake Fault Scientific Drilling project-hole 1 (WFSD-1). *Tectonophysics* **2014**, *619–620*, 86–100. [[CrossRef](#)]
19. Xue, L.; Li, H.; Brodsky, E.E.; Xu, Z.; Kano, Y.; Wang, H.; Mori, J.J.; Si, J.; Pei, J.; Zhang, W.; et al. Continuous permeability measurements record healing inside the Wenchuan earthquake fault zone. *Science* **2013**, *340*, 1555–1559. [[CrossRef](#)] [[PubMed](#)]
20. Salver-Disma, F.; Tarascon, J.M.; Clinard, C.; Rouzaud, J.N. Transmission electron microscopy studies on carbon materials prepared by mechanical milling. *Carbon* **1995**, *37*, 1941–1959. [[CrossRef](#)]
21. Sadezky, A.; Muckenhuber, H.; Grothe, H.; Niessner, R.; Poschl, U. Raman microspectroscopy of soot and related carbonaceous materials: Spectral analysis and structural information. *Carbon* **2005**, *43*, 1731–1742. [[CrossRef](#)]
22. Furuichi, H.; Ujiie, K.; Kouketsu, Y.; Saito, T.; Tsutsumi, A.; Wallis, S. Vitrinite reflectance and Raman spectra of carbonaceous material as indicators of frictional heating on faults: Constraints from friction experiments. *Earth Planet. Sci. Lett.* **2015**, *424*, 191–200. [[CrossRef](#)]
23. Lunsdorf, N.K.; Dunkl, I.; Schmidt, B.; Rantitsch, G.; von Eynatten, H. Towards a higher comparability of geothermometric data obtained by Raman spectroscopy of carbonaceous material. Part 1: Evaluation of biasing factors. *Geostand. Geoanal. Res.* **2014**, *38*, 73–94. [[CrossRef](#)]
24. Lunsdorf, N.K.; Dunkl, I.; Schmidt, B.; Rantitsch, G.; von Eynatten, H. Towards a higher comparability of geothermometric data obtained by Raman spectroscopy of carbonaceous material. Part 2: A revised geothermometer. *Geostand. Geoanal. Res.* **2017**, *41*, 593–612. [[CrossRef](#)]
25. Ferrari, A.C.; Robertson, J. Interpretation of Raman spectra of disordered and amorphous carbon. *Phys. Rev. B: Condens. Matter Mater. Phys.* **2000**, *61*, 14095–14107. [[CrossRef](#)]
26. Pastewka, L.; Moser, S.; Gumbsch, P.; Moseler, M. Anisotropic mechanical amorphization drives wear in diamond. *Nat. Mater.* **2011**, *10*, 34–38. [[CrossRef](#)] [[PubMed](#)]
27. Chen, J.; Niemeijer, A.; Yao, L.; Ma, S. Water vaporization promotes coseismic fluid pressurization and buffers temperature rise. *Geophys. Res. Lett.* **2017**, *44*, 2177–2185. [[CrossRef](#)]
28. Heermance, R.; Shipton, Z.K.; Evans, J.P. Fault structure control on fault slip and ground motion during the 1999 rupture of the Chelungpu Fault, Taiwan. *Seismol. Soc.* **2003**, *93*, 1034–1050. [[CrossRef](#)]
29. Isaacs, A.J.; Evans, J.P.; Song, S.-R.; Kolesar, P.T. Structural, mineralogical, and geochemical characterization of the Chelungpu Thrust Fault, Taiwan. *Terr. Atmos. Ocean. Sci.* **2007**, *18*, 183–221. [[CrossRef](#)]

30. Hirono, T.; Ikehara, M.; Otsuki, K.; Mishima, T.; Sakaguchi, M.; Soh, W.; Omori, M.; Lin, W.; Yeh, E.-C.; Tanikawa, W.; et al. Evidence of frictional melting within disk-shaped black materials discovered from the Taiwan Chelungpu fault system. *Geophys. Res. Lett.* **2006**, *33*, L19311. [[CrossRef](#)]
31. Kano, Y.; Mori, J.; Fujio, R.; Ito, H.; Yanagidani, T.; Nakao, S.; Ma, K.F. Heat signature on the Chelungpu fault associated with the 1999 Chi-Chi, Taiwan earthquake. *Geophys. Res. Lett.* **2006**, *33*, L14306. [[CrossRef](#)]
32. Kuo, L.-W.; Song, S.-R.; Yeh, E.-C.; Chen, H.-F. Clay mineral anomalies in the fault zone of the Chelungpu Fault, Taiwan, and their implications. *Geophys. Res. Lett.* **2009**, *36*, L18306. [[CrossRef](#)]
33. Kuo, L.-W.; Song, Y.F.; Yang, C.M.; Song, S.-R.; Wang, C.C.; Dong, J.J.; Suppe, J.; Shimamoto, T. Ultrafine spherical quartz formation during seismic fault slip: Natural and experimental evidence and its implications. *Tectonophysics* **2015**, *664*, 98–108. [[CrossRef](#)]
34. Chou, Y.-M.; Song, S.-R.; Aubourg, C.; Lee, T.-Q.; Boullier, A.-M.; Song, Y.-F.; Yeh, E.C.; Kuo, L.-W.; Wang, C.-Y. An earthquake slip zone is a magnetic recorder. *Geology* **2012**, *40*, 551–554. [[CrossRef](#)]
35. Rumble, D. Hydrothermal graphitic carbon. *Element* **2014**, *10*, 427–433. [[CrossRef](#)]
36. Kirilova, M.; Toy, V.; Rooney, J.S.; Giorgetti, C.; Gordon, K.C.; Collettini, C.; Takeshita, T. Structural disorder of graphite and implications for graphite thermometry. *Solid Earth* **2017**, *9*, 223–231. [[CrossRef](#)]
37. Sibson, R.H. Thickness of the seismic slip zone. *Seismol. Soc.* **2003**, *93*, 1169–1178. [[CrossRef](#)]
38. Di Toro, G.; Han, R.; Hirose, T.; De Paola, N.; Nielsen, S.; Mizoguchi, K.; Ferri, F.; Cocco, M.; Shimamoto, T. Fault lubrication during earthquakes. *Nature* **2011**, *471*, 494–498. [[CrossRef](#)] [[PubMed](#)]
39. Kumar, N.; Dash, S.; Tyagi, A.K.; Raj, B. Super low to high friction of turbostratic graphite under various atmospheric test conditions. *Tribol. Int.* **2011**, *22*, 1969–1978. [[CrossRef](#)]
40. Oohashi, K.; Hirose, T.; Shimamoto, T. Graphite as a lubricating agent in fault zones: An insight from low- to high-velocity friction experiments on a mixed graphite-quartz gouge. *J. Geophys. Res.* **2013**, *118*, 2067–2084. [[CrossRef](#)]
41. Ma, T.-B.; Wang, L.-F.; Hu, Y.-Z.; Li, X.; Wang, H. A shear localization mechanism for lubricity of amorphous carbon materials. *Sci. Rep.* **2014**, *4*, 3662. [[CrossRef](#)] [[PubMed](#)]
42. Ikari, M.J. Principle slip zone: Precursors but not recorders of earthquake slip. *Geology* **2015**, *43*, 955–958. [[CrossRef](#)]



© 2018 by the authors. Licensee MDPI, Basel, Switzerland. This article is an open access article distributed under the terms and conditions of the Creative Commons Attribution (CC BY) license (<http://creativecommons.org/licenses/by/4.0/>).